Mineralogical Magazine, February 2011, Vol. 75(1), pp. 65–86

The crystal chemistry of 'wheatsheaf' tourmaline from Mogok, Myanmar

A. J. Lussier[1], F. C. Hawthorne[1,*], Y. Abdu[1], S. Herwig[1], V. K. Michaelis[2], P. M. Aguiar[2] and S. Kroeker[2]

[1] Department of Geological Sciences, University of Manitoba, Winnipeg, Manitoba, Canada R3T 2N2
[2] Department of Chemistry, University of Manitoba, Winnipeg, Manitoba, Canada R3T 2N2

[*Received 22 August 2010; Accepted 21 December 2010*]

ABSTRACT

Tourmalines of unusual (mushroom) habit are common in granitic pegmatites of Momeik, northeast of Mogok, Myanmar. Here, we examine a sample of elbaite of significantly different habit, consisting of a series of diverging crystals, resembling a sheaf of wheat and ranging in colour from light purplish-red at the base to dark purplish-red at the tip with a thin green cap at the termination. The crystal structures of eight crystals are refined to R_1-indices of ~2.5% using graphite-monochromated Mo-$K\alpha$ X-radiation; the same crystals were analysed by electron microprobe. ^{11}B and ^{27}Al magic angle spinning nuclear magnetic resonance (MAS NMR) spectra were collected on four regions of the wheatsheaf crystal, and show ~0.3 a.p.f.u. $^{[4]}$B and <0.1 a.p.f.u. $^{[4]}$Al in the structure. ^{57}Fe Mössbauer spectroscopy was done on the dark green rim at the termination of the crystal, showing all Fe in this region (~0.6 a.p.f.u.) to be Fe^{2+}. Detailed electron-microprobe traverses show that the principal compositional variation involves the substitutions $^{[4]}B + {}^{Y}Al \rightarrow Si + {}^{Y}Fe^{*}$, where transition metals are present, and $^{[4]}B_2 + {}^{Y}Al \rightarrow Si_2 + {}^{Y}Li$, where transition metals are not present, although several other minor substitutions also affect crystal composition. Successive microscopic bifurcation of crystallites causes divergence of growth directions along the *c* axis, imparting the overall 'wheatsheaf' shape to the crystal aggregate. We suggest that such bifurcation is common in pegmatitic elbaite crystals, resulting in their common divergent habit.

Keywords: elbaite, Mogok, Myanmar, wheatsheaf, EPMA, Mössbauer spectroscopy, SEM, MAS-NMR spectroscopy.

Introduction

The Mogok region of Myanmar is well known as a centre for gem production and a wide variety of gemstones of both igneous and metamorphic origin come from this region (Themelis, 2007). The mines are located in a central belt of evolved tin-tungsten granites and associated topaz-bearing pegmatites that extends north–south through the country (Zaw, 1998; Barley *et al.*, 2003; Hla Kyi *et al.*, 2005). There has been considerable interest in the unusual mushroom-like habits of tourmaline from this region (Ertl *et al.*, 2007; Lussier *et al.*, 2008*a*,*b*) from the Kat Chai and Molo mines, and a wide variety of habits is available commercially.

The minerals of the tourmaline supergroup are common phases in a wide variety of rocks, and are of considerable use as indicator minerals. We may write the general chemical formula of tourmaline as

$$XY_3Z_6[T_6O_{18}][BO_3]_3V_3W$$

where X = Na, K, Ca, Pb^{2+}, Bi, □ (vacancy); Y = Li, Mg, Fe^{2+}, Mn^{2+}, Al, Cr^{3+}, V^{3+}, Fe^{3+}, Ti; Z = Mg, Fe^{2+}, Al, Fe^{3+}, V^{3+}, Cr^{3+}; T = Si, Al, B; B = B; V = OH, O; and W = OH, F, O.

* E-mail: frank_hawthorne@umanitoba.ca
DOI: 10.1180/minmag.2011.075.1.65

Chemical variations in tourmaline provide a record of crystallization of granitic and pegmatitic rocks (Aurisicchio *et al.*, 1999; Dyar *et al.*, 1998; Novák and Povondra, 1995; Novák *et al.*, 1999; Selway *et al.*, 1998, 1999, 2000*a*,*b*, 2002; Neiva *et al.*, 2007) and progressive metamorphism (Henry and Dutrow, 1992, 1996; Henry and Guidotti, 1985; Povondra and Novák, 1986) in a wide variety of rocks. Much work has been done on site occupancies in tourmaline (e.g. Hawthorne, 1996, 2002; Hawthorne *et al.*, 1993; Burns *et al.*, 1994; Grice and Ercit, 1993; Grice *et al.*, 1993; MacDonald and Hawthorne, 1995; MacDonald *et al.*, 1993; Taylor *et al.*, 1995; Dyar *et al.*, 1998; Francis *et al.*, 1999; Bloodaxe *et al.*, 1999; Cámara *et al.*, 2002; Schreyer *et al.*, 2002; Ertl and Hughes, 2002; Ertl *et al.*, 2003*a,b*, 2004, 2005; Hughes *et al.*, 2000, 2004; Marschall *et al.*, 2004; Bosi, 2008; Bosi and Lucchesi, 2004, 2007; Bosi *et al.*, 2004, 2005; Andreozzi *et al.*, 2008). The next step is to relate both compositional and complete site-population data with textural variations (habit, optical zonation) in tourmaline. In this study, we correlate the

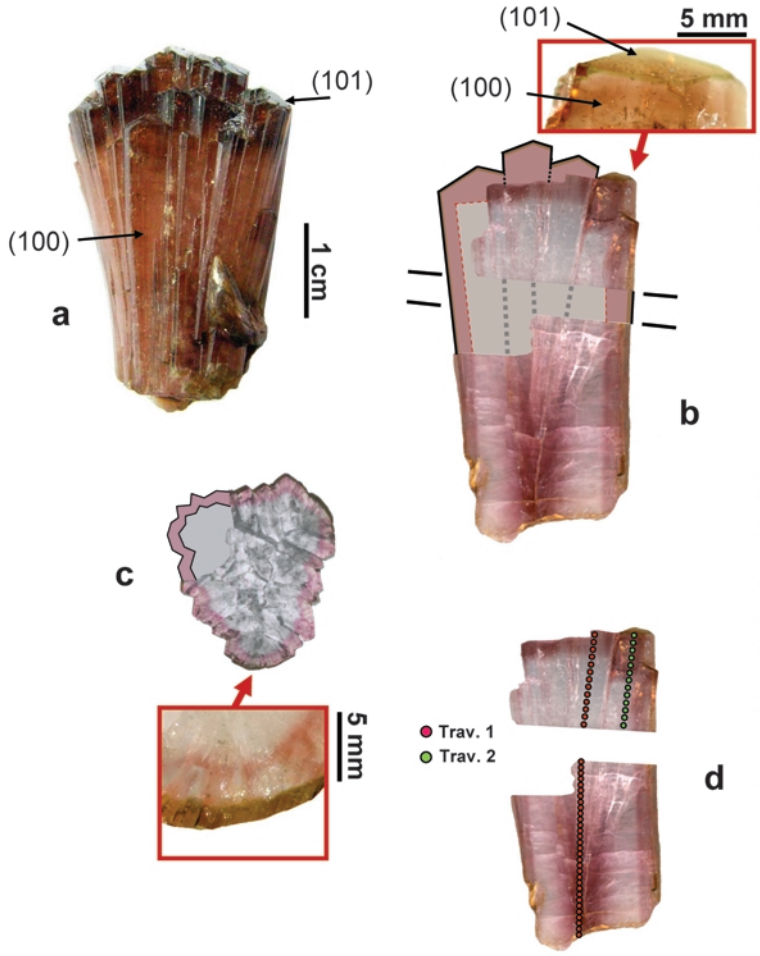

FIG. 1. Wheatsheaf tourmaline from Mogok: (*a*) entire sample; (*b*) doubly polished cross-section cut parallel to the *c* axis, shown in reflected light; the green layer on the end of crystal is shown enlarged in the red box (the section of the crystal removed for examination prior to photography was drawn schematically in uniform grey), and the pairs of parallel lines on either side show the location of the section shown in (*c*); (*c*) doubly polished section cut approximately perpendicular to the *c* axis and shown in transmitted light; the green rim is shown enlarged in the lower red box; (*d*) location of electron-microprobe traverses along a slab cut parallel to the *c* axis.

composition and ordering of cations over the tetrahedrally and octahedrally coordinated sites with variation in habit for wheatsheaf tourmaline from the Mogok region, Myanmar, using a combination of SREF, ^{11}B and ^{27}Al MAS NMR, Mössbauer spectroscopy, and EMPA (Electron MicroProbe Analysis).

Sample description

The sample examined here is a dense aggregate of euhedral crystals which diverge from base to termination in a manner somewhat resembling a sheaf of wheat, hence the name, 'wheatsheaf' (Fig. 1*a*). In hand specimen, the top (2–5 mm) of the sample is dark, opaque reddish-purple, and the rest of the sample is translucent reddish-brown. Cross sections parallel to and perpendicular to the average direction of the *c* axes of the crystals (Fig. 1*b*,*c*) reveal that the sample consists of many crystals that range between 1 and 3 mm across. These crystals can be traced throughout the length of the sample and display well formed terminations. Several longitudinal zones can be distinguished on the basis of colour and composition. At the base of the crystal is a dark red core that shows intense pleochroism from red to greenish-grey in transmitted plane-polarized light. This core changes gradually in the *c* direction (Figs 1, 2*a*) into a white-to-colourless region that forms the bulk of the sample, and microscopic bifurcation results in numerous tourmaline crystals the *c* axis of which are sub-parallel (see yellow lines in Fig. 2*b*). A sharp boundary separates the white zone from a dark reddish-pink rind, 2–3 mm thick, which envelops the entire sample (Fig. 1*b*,*c*). The outer edge of the sample consists of a very thin light- to dark-green rind, ranging in thickness from <0.5 to ~1 mm. This layer is discontinuous along the prism faces but is uniform on the terminal pyramid faces.

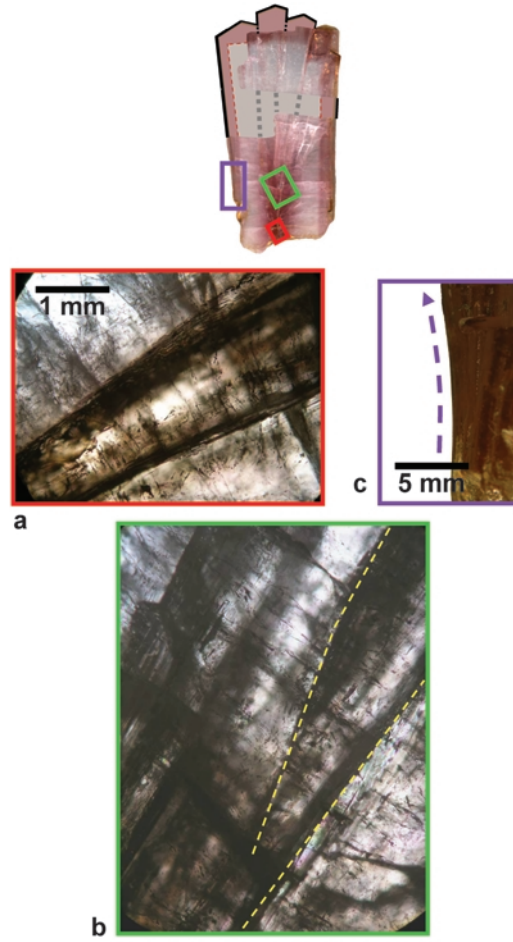

FIG. 2. Images of wheatsheaf tourmaline (from a doubly polished section) in plane-polarized light, showing (*a*) the central core zone at the base of the sample, (*b*) the central section of the sample where splitting of the initial core occurs, and (*c*) the edge of the sample showing the bent edge of a crystal.

Experimental methods

X-ray data collection

Eight single-crystal fragments were extracted from various different colour zones (see Table 1) of the sample for site-scattering refinement. SHW1 and SHW2 were ground to approximate spheres and mounted on thin, tapered glass fibres. The unit-cell dimensions of the crystals were determined using a Bruker *P*3 automated four-circle single-crystal diffractometer equipped with a serial detector and a Mo-*K*α X-ray source. The software used for data reduction and least-squares refinement is part of the *SHELXTL* PC package. For both crystals, twenty-five reflections between 10 and 30º2θ were centred using a random-search method. Data were collected from 4–60º2θ with an *hkl* index range from 0, 0, $\overline{11}$ to 23, 23, 11 at variable scan-speeds, depending on the intensity of the reflection; the scan range was set to 1.2º. An intense check-reflection was used to monitor intensity variation during data collection; no

TABLE 1. Data collection and refinement information for Mogok wheatsheaf tourmaline samples.

	SHW1	SHW2	SHW3	SHW4	SHW5	SHW6	SHW7	SHW8
a (Å)	15.7791(16)	15.7841(17)	15.8779(4)	15.8673(7)	15.8126(4)	15.7982(4)	15.8160(5)	15.7949(4)
c (Å)	7.0928(12)	7.0859(13)	7.1223(2)	7.1172(2)	7.1010(2)	7.0904(2)	7.0953(2)	7.0902(2)
V (Å^3)	1529.4(7)	1528.9(8)	1555.0(1)	1551.84(15)	1537.6(1)	1532.6(1)	1537.1(1)	1531.88(12)
Location	near surface, dark tip	near surface, light base	green cap, end	green cap, end	near surface, light base	white interior, middle	red core, base	red core, middle
Colour	purple-brown	light pink	green	dark green	red-purple	colourless	light pink/red	light pink/red
Crystal size	0.2 mm sphere	0.2 mm sphere	0.15 mm	0.1 mm block	0.1 mm	0.12 mm	0.08 mm	0.1 mm block
No. reflections > 10 σI	–	–	6612	6988	7146	7056	5559	7143
No. unique reflections	1107	974	1111	1090	1103	1097	1102	1095
R_1(obs) %	1.68	1.73	3.18	2.22	1.75	1.86	3.36	2.54
wR_2 %	4.33	4.41	7.34	5.36	4.49	4.63	7.10	5.91
GoF*	1.073	1.136	1.251	1.218	1.146	1.139	1.258	1.210
EXTI	0.0012(2)	0.0010(2)	—	——	—	——	——	——
R_1 / wR_2	1.70 / 4.40	1.72 / 4.37	3.26 / 7.51	2.39 / 5.83	1.77 / 4.59	1.93 / 4.89	3.35 / 7.31	2.67 / 6.41

Space group: $R3m$; $Z = 3$; Radiation/monochromator: Mo-$K\alpha$/Gr.

significant changes were observed. For both data sets, ψ-scan absorption corrections were done, together with the usual geometrical corrections, and the data were reduced to structure factors. The remaining six samples, SHW3 to SHW8, were mounted on tapered glass fibres as crystal fragments and analysed with Mo-$K\alpha$ X-radiation on a Bruker 4-circle diffractometer equipped with an APEX 4K CCD detector. In excess of a hemisphere of data was collected to 60º2θ using frame times of 10−60 s, depending on crystal size, and frame widths of 0.2º. Final unit-cell dimensions were determined on all reflections with $|I| > 10\sigma I$. Absorption corrections were carried out using *SADABS* (Sheldrick, 1998). The data were corrected for Lorentz, polarization and background effects, averaged and reduced to structure factors. The various data-collection and refinement parameters for all crystals are given in Table 1.

Crystal-structure refinement

Structure refinement was done with the *SHELTXL* (*version* 5.1) PC Plus software package in the space group *R*3*m*. Structures were tested for absolute orientation and transformed as appropriate. In the preliminary stages of refinement, the *Z*-site scattering did not diverge from full Al occupancy, and hence the *Z* site was fixed at full occupancy of Al in the final stages of refinement. The *Y* and *T* sites were constrained to be fully occupied by (Li + Al) and (Si + B), respectively, with the amounts of individual cations being variable. All samples were refined twice, first with the O(1) and O(2) sites fixed at (0, 0, *z*) and (x, $-x$, *z*), and second with these sites allowed to disorder at (x, $2x$, *z*) and (x, *y*, *z*), respectively. The second refinement was done to accommodate the high U_{eq} values observed for these sites in the completely ordered model, as discussed by Burns *et al*. (1994). All final refinements used a fully ionized scattering factor for O, and neutral scattering factors for the remaining species, as this gave the best agreement between *T*-site scattering values derived from compositional and structure-refinement data, as discussed by Lussier *et al*. (2011). As the O(1) site is occupied by F and (OH), for crystals where F > 0.5 a.p.f.u., the F scattering factor was used instead of the O^{2-} scattering factor at that site. Structure refinement using data collected by serial detector (SHW1 and SHW2) benefitted from the inclusion of an empirical isotropic-extinction parameter [of the form $k(1 + 0.001xF_c^2\lambda^3 / \sin2\theta)^{-1/4}$] whereas structures refined using data collected by CCD detector (SHW3-SHW8) did not. Furthermore, when included in the final least-squares cycles, extinction parameters repeatedly converged to zero for CCD-detector data.

Final R_1 and wR_2 indices are 1.68−3.32% and 4.33−7.34, respectively (Table 1). Refined atom positions and anisotropic-displacement parameters and selected interatomic distances are given in Tables 2 and 3, respectively; refined site-scattering values (Hawthorne *et al.*, 1995) are given in Table 4. The O(1) and O(2) positional parameters and corresponding *Y*−O distances are shown for ordered and disordered models; for all other parameters, differences between the ordered and disordered models are within the assigned standard deviations.

Electron-microprobe analysis

The crystals used for X-ray data collection were mounted in epoxy on 2.5 cm diameter Perspex® discs, ground and polished, carbon-coated and analysed with either a Cameca SX-50 (SHW1 and SHW2) or a Cameca SX-100 (SHW3 to SHW8) electron microprobe operating under the following conditions in wavelength-dispersion mode: excitation voltage: 15 kV, specimen current: 20 nA, beam size: 10 μm, peak count-time: 20 s, background count-time: 10 s. The following standards were used: TAP: andalusite (Al); diopside (Si); forsterite (Mg); LPET: orthoclase (K); diopside (Ca); titanite (Ti); LTAP: albite (Na); fluoro-riebeckite (F); LLiF: fayalite (Fe); spessartine (Mn); gahnite (Zn). The data were reduced and corrected by the PAP method of Pouchou and Pichoir (1985). Ten points on each crystal were analysed and backscattered-electron images of the crystals were examined to check for gross compositional zoning and inclusions; none was observed. The single slice removed from the green rim for Mössbauer spectroscopy was also analysed with a Cameca SX-100 electron microprobe operating under the same conditions and using the same standards. All chemical compositions are listed in Table 5 and all correspond to elbaite (Hawthorne and Henry, 1999).

To assess compositional variation throughout the entire wheatsheaf sample, a section was cut parallel to the *c* axis and polished, and electron microprobe data were collected along two traverses across the polished slab (Fig. 1*d*) with the same settings and standards as listed above.

TABLE 2. Positional and equivalent anisotropic-displacement parameters for Mogok wheatsheaf tourmaline samples.

		SHW1	SHW2	SHW3	SHW4	SHW5	SHW6	SHW7	SHW8
X	*x*	0	0	0	0	0	0	0	0
	y	0	0	0	0	0	0	0	0
	z	0.2313(3)	0.2314(3)	0.2342(5)	0.2323(4)	0.2294(2)	0.2317(3)	0.2332(4)	0.2307(3)
	U_{eq}	0.0183(5)	0.0170(5)	0.0236(10)	0.0242(7)	0.0208(5)	0.0197(7)	0.015(1)	0.0151(7)
Y	*x*	0.12326(7)	0.12352(8)	0.12382(11)	0.12377(8)	0.12383(8)	0.12312(8)	0.12300(15)	0.12314(11)
	y	1/2*x*	1/2*x*	1/2*x*	1/2*x*	1/2*x*	1/2*x*	1/2*x*	1/2*x*
	z	0.63487(15)	0.63598(19)	0.6306(2)	0.63092(17)	0.63562(16)	0.63673(17)	0.6368(3)	0.6380(2)
	U_{eq}	0.0102(3)	0.0104(4)	0.0131(4)	0.0129(3)	0.0129(3)	0.0101(3)	0.0104(6)	0.0105(5)
Z	*x*	0.29696(3)	0.29695(3)	0.29732(6)	0.29737(5)	0.29701(3)	0.29680(4)	0.29681(6)	0.29689(5)
	y	0.26017(3)	0.26011(3)	0.26024(7)	0.26033(5)	0.26003(3)	0.26016(4)	0.26003(6)	0.26010(5)
	z	0.61030(9)	0.61035(10)	0.61167(17)	0.61159(12)	0.61059(9)	0.60965(10)	0.61017(17)	0.61008(14)
	U_{eq}	0.00660(11)	0.00727(12)	0.00824(19)	0.00867(13)	0.00929(10)	0.00850(11)	0.00717(18)	0.00826(15)
T	*x*	0.19168(3)	0.19173(3)	0.19190(5)	0.19185(4)	0.19171(3)	0.19156(3)	0.19179(5)	0.19161(4)
	y	0.18976(3)	0.18975(3)	0.19001(6)	0.19001(4)	0.18983(3)	0.18961(3)	0.18979(6)	0.18971(5)
	z	0	0	0	0	0	0	0	0
	U_{eq}	0.00540(14)	0.00598(15)	0.0057(2)	0.00670(17)	0.00722(13)	0.00692(14)	0.0057(2)	0.00641(19)
B	*x*	0.10896(9)	0.10889(9)	0.10934(19)	0.10936(13)	0.10911(9)	0.10902(10)	0.10898(18)	0.10917(15)
	y	2*x*	2*x*	2*x*	2*x*	2*x*	2*x*	2*x*	2*x*
	z	0.4552(3)	0.4551(4)	0.4557(6)	0.4555(5)	0.4556(3)	0.4541(4)	0.4538(6)	0.4541(5)
	U_{eq}	0.0070(4)	0.0081(4)	0.0104(8)	0.0105(6)	0.0104(4)	0.0094(4)	0.0093(8)	0.0102(6)
O(1)[d]	*x*	0.0178(4)	0.0175(4)	0.0231(5)	0.0225(4)	0.0183(4)	0.0160(5)	0.0166(9)	0.0167(7)
	y	1/2*x*	1/2*x*	1/2*x*	1/2*x*	1/2*x*	1/2*x*	1/2*x*	1/2*x*
	z	0.7826(5)	0.7822(6)	0.7873(9)	0.7864(7)	0.7833(5)	0.7816(5)	0.7830(9)	0.7822(7)
	U_{eq}	0.0084(10)	0.0095(12)	0.0165(19)	0.0170(14)	0.0217(11)	0.0097(12)	0.023(2)	0.0213(18)
O(1)[o]	*x*	0	0	0	0	0	0	0	0
	y	0	0	0	0	0	0	0	0
	z	0.7825(5)	0.7821(6)	0.787(1)	0.7860(7)	0.7831(5)	0.7814(5)	0.7829(9)	0.7822(7)
	U_{eq}	0.0311(9)	0.0315(9)	0.058(2)	0.0560(16)	0.0459(9)	0.0273(8)	0.0426(16)	0.0406(12)
O(2)[d]	*x*	0.0527(3)	0.0525(3)	0.0511(4)	0.0515(3)	0.0521(2)	0.0531(3)	0.0520(5)	0.0520(4)
	y	0.9323(3)	0.9325(3)	0.9300(4)	0.9304(3)	0.9321(2)	0.9329(3)	0.9319(5)	0.9322(4)
	z	0.4868(2)	0.4867(3)	0.4846(5)	0.4848(3)	0.4867(2)	0.4881(3)	0.4859(5)	0.4860(4)
	U_{eq}	0.0108(5)	0.0110(5)	0.0102(8)	0.0109(6)	0.0125(5)	0.0122(5)	0.0105(9)	0.0118(7)
O(2)[o]	*x*	0.06015(6)	0.05995(7)	0.06053(12)	0.06050(9)	0.05999(6)	0.06004(7)	0.06001(12)	0.05987(9)
	y	2*x*	2*x*	2*x*	2*x*	2*x*	2*x*	2*x*	2*x*
	z	0.4866(3)	0.4866(3)	0.4844(5)	0.4846(4)	0.4865(3)	0.4880(3)	0.4858(5)	0.4859(4)
	U_{eq}	0.0158(4)	0.0164(4)	0.0188(8)	0.0187(6)	0.0181(4)	0.0166(4)	0.0164(7)	0.0173(6)
O(3)	*x*	0.26611(14)	0.26600(15)	0.2687(3)	0.26835(18)	0.26625(14)	0.26466(15)	0.2660(3)	0.2651(2)
	y	1/2*x*	1/2*x*	1/2*x*	1/2*x*	1/2*x*	1/2*x*	1/2*x*	1/2*x*
	z	0.5085(2)	0.5088(3)	0.5109(4)	0.5108(3)	0.5100(2)	0.5079(2)	0.5088(4)	0.5088(3)
	U_{eq}	0.0121(3)	0.0125(3)	0.0113(6)	0.0124(4)	0.0146(3)	0.0137(4)	0.0130(6)	0.0134(5)
O(4)	*x*	0.09303(6)	0.09302(6)	0.09283(12)	0.09295(8)	0.09297(6)	0.09336(7)	0.09304(12)	0.09296(10)
	y	2*x*	2*x*	2*x*	2*x*	2*x*	2*x*	2*x*	2*x*
	z	0.0735(2)	0.0743(3)	0.0722(4)	0.0725(3)	0.0741(2)	0.0736(3)	0.0742(4)	0.0742(4)
	U_{eq}	0.0092(3)	0.0104(3)	0.0113(6)	0.0114(4)	0.0123(3)	0.0120(3)	0.0114(6)	0.0121(5)
O(5)	*x*	0.18581(13)	0.18566(13)	0.1860(2)	0.18597(17)	0.18569(13)	0.18644(14)	0.1860(2)	0.1855(2)
	y	1/2*x*	1/2*x*	1/2*x*	1/2*x*	1/2*x*	1/2*x*	1/2*x*	1/2*x*
	z	0.0951(2)	0.0952(3)	0.0944(4)	0.0943(3)	0.0952(2)	0.0960(2)	0.0964(4)	0.0961(3)
	U_{eq}	0.0094(3)	0.0105(3)	0.0111(6)	0.0117(4)	0.0127(3)	0.0123(3)	0.0110(6)	0.0125(5)

Table 2 (*contd*.)

		SHW1	SHW2	SHW3	SHW4	SHW5	SHW6	SHW7	SHW8
O(6)	x	0.19537(8)	0.19515(8)	0.19662(15)	0.19639(10)	0.19521(8)	0.19499(8)	0.19513(15)	0.19481(12)
	y	0.18540(8)	0.18514(8)	0.18653(15)	0.18640(10)	0.18522(8)	0.18452(8)	0.18473(15)	0.18459(12)
	z	0.77569(17)	0.77550(18)	0.7755(3)	0.7760(2)	0.77589(17)	0.77494(18)	0.7745(3)	0.7750(3)
	U_{eq}	0.0079(2)	0.0083(2)	0.0094(4)	0.0098(3)	0.0104(2)	0.0094(2)	0.0092(4)	0.0095(3)
O(7)	x	0.28587(8)	0.28600(8)	0.28553(14)	0.28550(10)	0.28585(8)	0.28613(8)	0.28617(14)	0.28610(12)
	y	0.28560(7)	0.28558(8)	0.28567(14)	0.28562(10)	0.28557(7)	0.28578(8)	0.28580(14)	0.28564(11)
	z	0.07885(15)	0.07905(17)	0.0803(3)	0.0804(2)	0.07927(15)	0.07811(17)	0.0789(3)	0.0784(2)
	U_{eq}	0.00699(19)	0.0076(2)	0.0076(4)	0.0085(3)	0.0091(2)	0.0086(2)	0.0076(4)	0.0084(3)
O(8)	x	0.20956(8)	0.20965(8)	0.20987(16)	0.20980(11)	0.20963(8)	0.20963(9)	0.20974(15)	0.20954(12)
	y	0.26992(8)	0.26990(9)	0.27044(16)	0.27037(11)	0.26995(8)	0.26992(9)	0.26991(16)	0.26979(13)
	z	0.43964(16)	0.43979(19)	0.4413(3)	0.4414(2)	0.44037(16)	0.43866(18)	0.4394(3)	0.4390(2)
	U_{eq}	0.0077(2)	0.0082(2)	0.0103(4)	0.0104(3)	0.0099(2)	0.0095(2)	0.0087(4)	0.0091(3)
H(3)	x	0.257(2)	0.249(3)	0.271(4)	0.270(3)	0.256(2)	0.255(2)	0.255(4)	0.254(3)
	y	1/2*x*	1/2*x*	1/2*x*	1/2*x*	1/2*x*	1/2*x*	1/2*x*	1/2*x*
	z	0.374(3)	0.378(3)	0.375(3)	0.376(3)	0.377(3)	0.376(3)	0.376(3)	0.376(3)
	U_{eq}	0.015	0.015	0.015	0.015	0.015	0.015	0.015	0.015

Magic-angle-spinning nuclear magnetic resonance spectroscopy

Material was extracted from various different colour zones of the sample for spectroscopic examination. The MAS NMR spectra of ^{27}Al (ν_L = 156.3 MHz) and ^{11}B (ν_L = 192.4 MHz) were recorded using a Varian Unity Inova® 600 spectrometer (B_o = 14.1 T). Between 10 and 35 mg of powdered sample (~15 μm crystallites) was placed in a 3.2 mm (22 μl capacity) zirconia rotor and spun at 18 to 20 (±0.005) kHz in a Varian-CHEMAGNETICS double-resonance probe. The optimized recycle delay was determined independently for each sample; averages were 7 and 3 s for ^{27}Al and ^{11}B, respectively. The final spectra are composites of 1024 to 3072 averaged scans and were referenced to 0.1 M H_3BO_3 as a secondary reference (= +19.6 ppm with respect to $BF_3(CH_3CH_2)_2O$), and 1.1 M $Al(NO_3)_3$. Pulse widths were selected to coincide approximately with a 10° tip angle at an rf nutation frequency of 50 kHz, thus ensuring quantitative peak intensities. ^{11}B MAS NMR spectra were also acquired at ultra high field (21.1 T; ν_L = 288.8 MHz) on an Avance II 900 spectrometer using a 2.5 mm double-resonance Bruker probe at sample-spinning rates of 30 kHz. Due to a strong ^{11}B background signal from BN in the probe, single-pulse (Bloch-decay) spectra were unusable. Instead, rotor-synchronized Hahn-echo spectra were collected with ν_{rf} = 62.5 kHz, recycle delays of 1 s, and 175 co-added transients. This approach yielded reliable peak positions, but compromised the precision of the relative peak intensities.

Mössbauer spectroscopy

Part of the green rim was removed from one of the crystals by slicing a thin (~1 mm) sheet parallel to the flat crystal face (SHW1-GC). The sample was ground with an agate mortar and pestle, placed on a Pb ring (2 mm inner diameter), and secured in place with tape. A Mössbauer spectrum was acquired in transmission geometry using a $^{57}Co(Rh)$ point source. The spectrometer was calibrated with the room-temperature spectrum of α-Fe. The spectra were analysed by a Voigt-function-based quadrupole-splitting distribution method using the RECOIL® software package.

Results and discussion

^{11}B MAS NMR spectra

It has been shown that MAS NMR is sensitive to coordination number for Al and B in the tourmaline structure (Tagg *et al.*, 1999; Schreyer *et al.*, 2002; Marler and Ertl, 2002; Lussier *et al.*, 2008*a*, 2009) in which the amounts of paramagnetic elements are sufficiently low to prevent signal attenuation (i.e. <0.1 a.p.f.u. Mn + Fe). In all parts of the wheatsheaf tourmaline, the

TABLE 3. Selected interatomic distances (Å) for Mogok wheatsheaf tourmaline samples.

	SHW1	SHW2	SHW3	SHW4	SHW5	SHW6	SHW7	SHW8
X–O(2) ×3	2.450(2)	2.445(2)	2.445(4)	2.453(3)	2.461(2)	2.453(3)	2.437(4)	2.445(3)
X–O(4) ×3	2.778(2)	2.776(2)	2.802(3)	2.797(3)	2.775(2)	2.790(2)	2.787(4)	2.775(3)
X–O(5) ×3	2.717(2)	2.715(2)	2.744(3)	2.738(3)	2.716(2)	2.726(2)	2.726(3)	2.711(3)
<*X*–O>	2.648	2.645	2.664	2.663	2.651	2.656	2.650	2.644
Y–O(1)[d] ×⅓	1.782(5)	1.782(5)	1.778(7)	1.778(5)	1.785(5)	1.790(6)	1.79(1)	1.779(9)
Y–O(1)[d] ×⅔	2.098(3)	2.094(4)	2.188(5)	2.177(4)	2.113(3)	2.075(4)	2.085(8)	2.078(6)
Y–O(2)[d]	1.882(3)	1.886(3)	1.871(5)	1.874(4)	1.886(3)	1.889(4)	1.887(6)	1.891(5)
Y–O(2)[d]	2.059(3)	2.062(3)	2.094(5)	2.087(4)	2.072(3)	2.053(4)	2.076(6)	2.074(5)
Y–O(3)	2.148(2)	2.146(2)	2.167(4)	2.163(3)	2.145(2)	2.141(2)	2.158(4)	2.147(3)
Y–O(6) ×2	1.971(1)	1.961(1)	2.007(2)	2.005(2)	1.967(1)	1.954(1)	1.957(3)	1.950(2)
Y–O(1)[o]	1.983(2)	1.981(3)	2.034(4)	2.027(3)	1.993(2)	1.972(2)	1.978(4)	1.970(3)
Y–O(2)[o] ×2	1.969(1)	1.972(2)	1.980(2)	1.978(2)	1.977(1)	1.970(1)	1.980(3)	1.981(2)
Y–O(3)	2.147(2)	2.145(2)	2.167(4)	2.163(3)	2.144(2)	2.140(2)	2.158(4)	2.147(3)
Y–O(6) ×2	1.971(1)	1.961(1)	2.007(2)	2.005(2)	1.967(1)	1.954(1)	1.957(3)	1.950(2)
<*Y*–O[o]>	2.002	1.999	2.029	2.026	2.004	1.993	2.002	1.997
Z–O(3)	1.9506(8)	1.9497(9)	1.952(2)	1.952(1)	1.9488(9)	1.9572(9)	1.953(2)	1.953(1)
Z–O(6)	1.856(1)	1.857(1)	1.848(2)	1.853(2)	1.861(1)	1.862(1)	1.857(2)	1.862(2)
Z–O(7)	1.882(1)	1.881(1)	1.886(2)	1.884(2)	1.884(1)	1.883(1)	1.884(2)	1.885(2)
Z–O(7)	1.945(1)	1.945(1)	1.960(2)	1.959(2)	1.951(1)	1.943(1)	1.947(2)	1.944(2)
Z–O(8)	1.880(1)	1.879(1)	1.882(2)	1.882(2)	1.883(1)	1.881(1)	1.882(2)	1.880(2)
Z–O(8)	1.898(1)	1.896(1)	1.911(2)	1.909(2)	1.900(1)	1.898(1)	1.899(2)	1.900(2)
<*Z*–O>	1.902	1.901	1.907	1.907	1.905	1.904	1.904	1.904
T–O(4)	1.6148(7)	1.6176(7)	1.623(1)	1.6220(9)	1.6194(7)	1.6156(7)	1.621(1)	1.617(1)
T–O(5)	1.6303(8)	1.6304(9)	1.640(2)	1.639(1)	1.6346(8)	1.6327(8)	1.637(1)	1.634(1)
T–O(6)	1.595(1)	1.595(1)	1.603(2)	1.598(2)	1.595(1)	1.600(1)	1.6042(2)	1.600(2)
T–O(7)	1.600(1)	1.602(1)	1.608(2)	1.607(1)	1.604(1)	1.605(1)	1.607(2)	1.603(2)
<*T*–O>	1.610	1.611	1.619	1.617	1.613	1.613	1.617	1.614
B–O(2)	1.357(3)	1.361(3)	1.365(6)	1.365(4)	1.368(3)	1.366(3)	1.366(6)	1.373(5)
B–O(8) ×2	1.379(2)	1.382(2)	1.386(3)	1.384(2)	1.381(2)	1.381(2)	1.384(3)	1.377(3)
<*B*–O>	1.372	1.375	1.379	1.378	1.377	1.376	1.378	1.376

TABLE 4. Site-scattering values (e.p.f.u.) for Mogok wheatsheaf tourmaline samples derived from SREF and EMPA.

	X site		*Y* site		*T* site	
	SREF	EMPA	SREF	EMPA	SREF	EMPA
SHW1	10.8(1)	10.0	28.3(2)	26.8	81.4(3)	82.0
SHW2	12.0(1)	11.3	26.7(2)	26.1	81.5(4)	81.6
SHW3	12.4(2)	11.1	36.8(3)	37.7	81.3(5)	83.1
SHW4	12.3(1)	11.8	36.5(2)	37.0	81.6(4)	82.8
SHW5	12.4(1)	11.5	27.1(2)	27.0	80.6(3)	80.6
SHW6	10.1(1)	9.9	27.0(2)	26.3	79.0(3)	80.4
SHW7	11.0(2)	11.4	26.3(3)	26.2	80.0(5)	81.5
SHW8	12.2(1)	12.3	27.0(2)	26.4	79.3(4)	78.8
<dev.>	0.6	0.6	0.9			

TABLE 5. Chemical composition (wt.%) and unit formulae* (a.p.f.u.) for Mogok wheatsheaf tourmaline samples.

	SHW1	SHW2	SHW3	SHW4	SHW5	SHW6	SHW7	SHW8	SHWGC
SiO_2	37.64	37.25	36.48	36.31	36.46	35.96	36.39	35.27	36.27
Al_2O_3	41.84	41.71	37.20	37.31	40.90	42.09	42.41	42.71	37.41
TiO_2	0.21	0.02	0.67	0.64	0.12	0.00	0.03	0.03	0.52
Fe_2O_3	–	–	0.29	0.27	–	–	–	–	0.23
FeO	0.25	0.04	4.95	4.58	0.22	0.01	0.01	0.01	4.03
MnO	0.33	0.46	0.18	0.20	0.64	0.03	0.27	0.22	0.32
ZnO	0.00	0.00	0.08	0.08	0.00	0.00	0.00	0.00	0.00
CaO	1.21	1.65	0.33	0.44	1.40	1.16	1.93	2.38	0.67
Na_2O	1.84	1.78	2.89	2.85	2.04	1.82	1.56	1.41	2.75
F	0.86	0.85	1.38	1.58	1.39	0.99	1.15	1.19	1.41
Li_2O	2.16	2.22	1.76	1.80	2.16	2.06	2.17	2.12	1.86
B_2O_3	12.18	12.32	10.92	10.93	11.73	11.83	12.19	12.90	11.28
H_2O*	3.50	3.50	3.05	2.95	3.15	3.34	3.33	3.32	3.04
O=F	−0.36	−0.36	−0.58	−0.67	−0.59	−0.42	−0.48	−0.50	−0.59
Total	101.65	101.44	99.60	99.28	99.63	98.87	100.96	101.06	99.20
Si	5.775	5.729	5.898	5.881	5.736	5.663	5.627	5.444	5.854
B	0.225	0.271	0.048	0.059	0.186	0.216	0.254	0.437	0.143
Al	–	–	0.054	0.056	0.078	0.121	0.119	0.119	0.003
Σ*T*	6.000	6.000	6.000	6.000	6.000	6.000	6.000	6.000	6.000
^{Z}Al	6	6	6	6	6	6	6	6	6
^{Y}Al	1.566	1.561	1.035	1.059	1.506	1.691	1.610	1.651	1.114
Ti	0.024	0.002	0.081	0.078	0.014	0.000	0.003	0.003	0.063
Fe^{3+}	–	–	0.035	0.033	–	–	–	–	0.028
Fe^{2+}	0.032	0.005	0.669	0.622	0.029	0.001	0.001	0.001	0.544
Mn^{2+}	0.043	0.060	0.025	0.027	0.085	0.004	0.035	0.029	0.044
Zn	0.000	0.000	0.010	0.010	0.000	0.000	0.000	0.000	0.000
Li	1.333	1.373	1.144	1.172	1.367	1.305	1.349	1.316	1.207
Σ*Y*	2.998	3.001	2.999	3.001	3.001	3.001	2.998	3.000	3.000
Na	0.547	0.531	0.906	0.895	0.662	0.556	0.468	0.422	0.861
Ca	0.199	0.272	0.057	0.076	0.236	0.196	0.320	0.394	0.116
Σ*X*	0.746	0.803	0.963	0.971	0.898	0.752	0.788	0.816	0.977
OH	3.583	3.587	3.289	3.187	3.308	3.507	3.438	3.419	3.273
F	0.417	0.413	0.706	0.809	0.692	0.493	0.562	0.581	0.720

* determined by stoichiometry
Formula contents on a basis of 31 anions.

paramagnetic contents are quite low (Table 5) and the spectra of both ^{11}B and ^{27}Al are well resolved over the regions of interest (Figs 3−5).

All ^{11}B spectra (Fig. 3) show strong peaks centred at ~14 ppm corresponding to $^{[3]}$B (Kroeker and Stebbins, 2001), and a prominent, sharp peak at ~0 ppm, corresponding to $^{[4]}$B. In principle, the ratio of the intensities of the signals from $^{[3]}$B and $^{[4]}$B gives the relative amounts of these species (Bray, 1999, Michaelis *et al.*, 2007), provided there is minimal differential interaction with paramagnetic species. In tourmaline, the amount of $^{[3]}$B is known exactly (3.0 a.p.f.u.) and hence the amount of $^{[4]}$B may be derived. Calculation of all ^{11}B MAS NMR spectra collected at 14.1 T was done using the time-domain density-matrix calculation program, *STARS* (Skibsted *et al.*, 1991), as implemented in the spectrometer software.

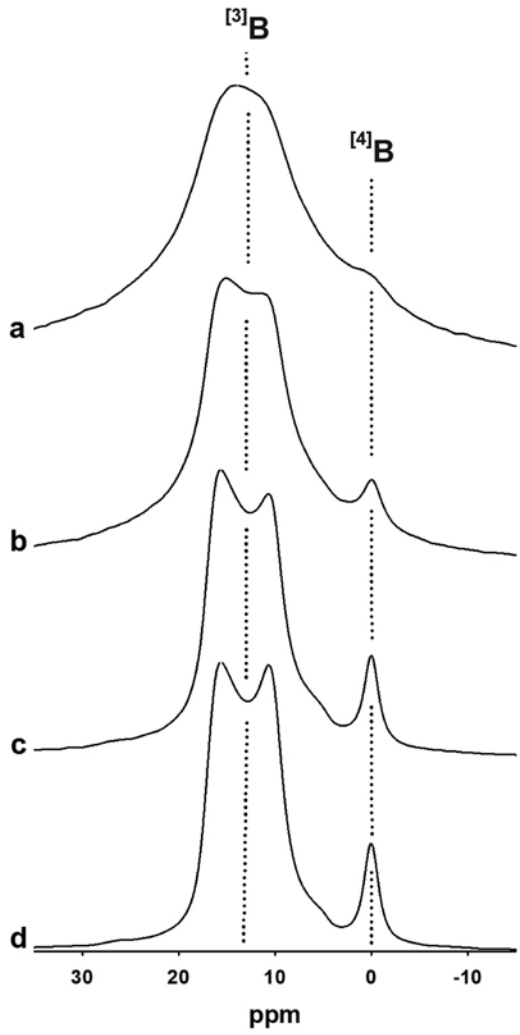

FIG. 3. ^{11}B MAS NMR spectra of wheatsheaf tourmaline: (*a*) SHW-NMR1 (purple tip); (*b*) SHW-NMR2 (purple brown); (*c*) SHW-NMR3 (white centre); (*d*) SHW-NMR4 (red core). The positions of the peaks corresponding to [3]-coordinate B and [4]-coordinate B are marked.

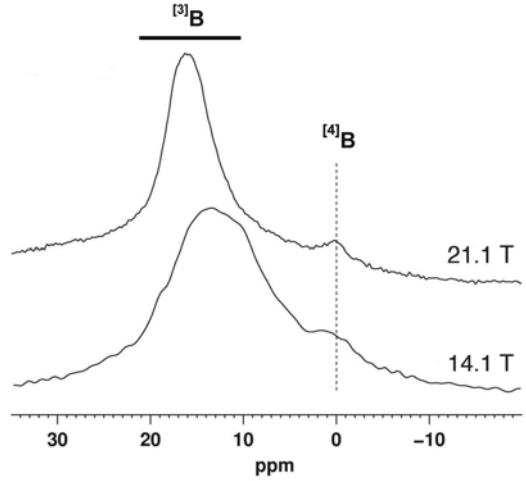

FIG. 4. Comparison of ^{11}B MAS NMR spectra of wheatsheaf tourmaline (sample similar to SHW-NMR2) collected at high field (14.1 T) and ultrahigh (21 T) field strength.

Isotropic chemical shifts (δ_{iso}), quadrupole coupling constants (C_Q), and quadrupolar asymmetry parameters (η) were obtained for the different *B* sites by manual adjustment of these NMR parameters for all transitions, beginning with the values obtained for elbaite and liddicoatite tourmalines by Tagg *et al.* (1999) and Lussier *et al.* (2008*a*). For each spectrum, the same value of Lorentzian line-broadening (150−700 Hz) was added for both *B* sites in order to improve agreement between the observed and simulated spectra. Simulated values of $^{[4]}$B in wheatsheaf tourmaline averaged 0.3 a.p.f.u. All simulation parameters and results are reported in Table 6. For both simulations and peak-fitting (see below for Al), fits were evaluated by visual comparison between experimental and calculated spectra, and uncertainties assessed by altering given parameters to the threshold of reasonable agreement. Intensities were converted into site populations using $^{[4]}B = 3 \times {}^{[4]}I^{B} / {}^{[3]}I^{B}$ a.p.f.u. and $^{[4]}Al = Al_{total} \times {}^{[4]}I^{Al} / ({}^{[4]}I^{Al} + {}^{[6]}I^{Al})$ a.p.f.u. as explained in Lussier *et al.* (2009). Relative errors for individual spectra are as given in Table 6 and were estimated by examining the variation of repeated simulation and fitting attempts.

Spectra at ultrahigh field strength (21.1 T) show the expected narrowing of the $^{[3]}$B signal and accompanying shift of the centre-of-gravity to higher frequency (i.e. nearer the isotropic chemical shift). This results in enhanced resolution of the $^{[3]}$B and $^{[4]}$B signals (Fig. 4). However, overlap with an intense broad signal arising from boron-nitride components in the probe reduced the accuracy of the quantities obtained.

^{27}Al MAS NMR spectra

The peak centred at ~0 ppm (Fig. 5) corresponds to $^{[6]}$Al at the *Y* and Z sites (Lussier *et al.*, 2008*a*,

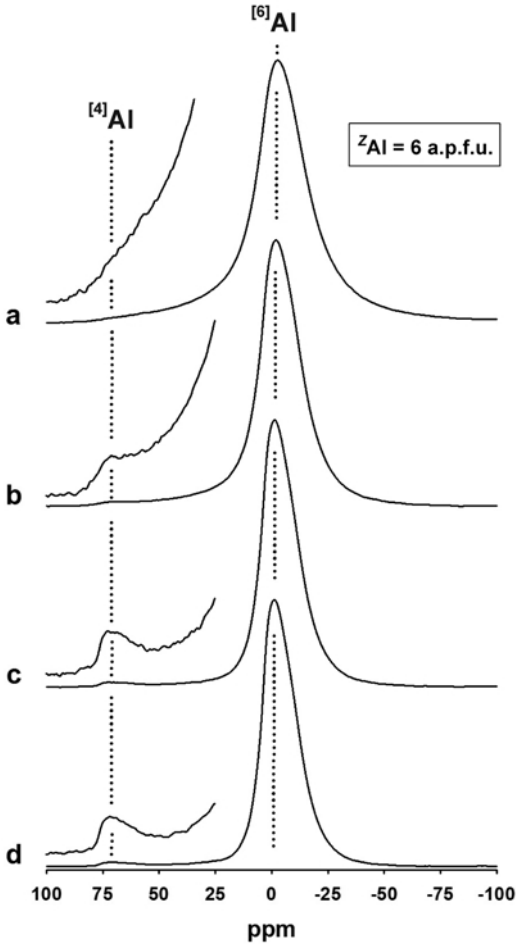

FIG. 5. ^{27}Al MAS NMR spectra of wheatsheaf tourmaline: (*a*) SHW-NMR1 (purple tip); (*b*) SHW-NMR2 (purple brown); (*c*) SHW-NMR3 (white centre); and (*d*) SHW-NMR4 (red core). The positions of the peaks corresponding to [4]- and [6]-coordinated Al are marked by dotted lines, and the spectra are shown with an increased intensity scale in the vicinity of signals assigned to [4]-coordinated Al.

2009). The ^{27}Al MAS NMR spectra lack the well defined lineshapes required to obtain NMR parameters, but could be adequately modelled by asymmetric Lorentzian-Gaussian peakshapes from which the integrated intensities could be determined. In all samples, $^{[4]}$Al is visible in the 60−75 ppm region, and the results of peak fitting (averages of five fittings of each spectrum) indicate that <2% of the total Al is [4]-coordinated. For the average tourmaline composition here (Table 5), this corresponds to <0.12 a.p.f.u. Substantial uncertainty is associated with ^{27}Al peak fitting for these tourmalines. This is due to the asymmetric nature of all peaks, the broad base of the ~0 ppm peak, and the relative sizes of the ~65 and 0 ppm peaks.

Formula calculation

If analysis for H, B and Li is not done, some assumptions are necessary concerning their presence in the structure when calculating the chemical formula. Typically, one sets (OH + F) = 4 a.p.f.u., B = 3 a.p.f.u., and ^{Y}Li = 9 − Σ (*Y* + *Z*) a.p.f.u., and calculates the formula on the basis of 31 anions with these constraints (e.g. Burns *et al.*, 1994). However, the ^{11}B and ^{27}Al MAS NMR spectra indicate the presence of significant amounts of $^{[4]}$B and $^{[4]}$Al throughout the sample crystal. The formula was normalized on 31 anions with (OH + F) = 4 a.p.f.u. and ^{Y}Li = 9 − Σ (*Y* + *Z*) a.p.f.u., and we incorporated $^{[4]}$B and $^{[4]}$Al into the calculation in the following way: for each crystal, the amount of B_2O_3 in the formula was calculated by iteration such that the content of the *T* site is Si + $^{[4]}$B + $^{[4]}$Al = 6 a.p.f.u. and $^{[4]}$Al is in accord with the amount of $^{[4]}$Al determined by ^{27}Al MAS-NMR spectroscopy (Table 6). For crystals SHW3 and SHW4, we have no MAS NMR results as these crystals contain sufficient transition metals (paramagnetic species) to quench the signal. However, the <*T*−O> distances of 1.618 Å (Table 3) indicate approximately equal amounts of $^{[4]}$B and $^{[4]}$Al, and the formulae (Table 5) were calculated accordingly.

Site populations

The <$^{[3]}$B−O> distances vary between 1.372 and 1.380 Å (Table 3) with a grand mean value of 1.377 Å. These values are close to the grand <$^{[3]}$B−O> distance in minerals of 1.370 Å given by Hawthorne *et al*. (1996), indicating complete occupancy of the *B* site by B.

The ^{11}B and ^{27}Al MAS NMR spectra (Figs 3, 5) show the presence of small amounts of $^{[4]}$B and $^{[4]}$Al in all crystals examined here. Lussier *et al.* (2011) examined the relation between <*T*−O> and the aggregate radius of the constituent *T*-site cations; this relation is shown in Fig. 7*a* with the data from the present study shown as large red circles. Two lines through the data are shown in Fig. 7*a*, a dashed line which was drawn through all the data (except those of the present study) and

TABLE 6. ^{11}B and ^{27}Al MAS NMR sample locations and parameters for Mogok wheatsheaf tourmaline samples.

Sample	Location	Site	δ_{iso} (ppm)	C_Q (MHz)	η	Peak intensity (rel.%)	$^{[4]}$B (a.p.f.u.)	%$^{[4]}$Al	$^{[4]}$Al (a.p.f.u.)
SHW-NMR1	Purple tip	$^{[3]}$B	18.7±1	2.9±0.3	0.2±0.2	91±4	0.30±0.14	<<1	—
		$^{[4]}$B	0±1	0.3*	1*	9±4			
SHW-NMR2	Purple brown	$^{[3]}$B	18.5±1	2.9±0.2	0.1±0.1	92±2	0.26±0.07	1.1(9)	0.08(7)
		$^{[4]}$B	0±0.5	0.3*	1*	8±2			
SHW-NMR3	White centre	$^{[3]}$B	18.5±0.5	2.88±0.1	0.1±0.1	91±1	0.30±0.03	2(1)	0.12(8)
		$^{[4]}$B	0.1±0.5	0.3*	1*	9±1			
SHW-NMR4	Red core	$^{[3]}$B	18.5±0.5	2.9±0.1	0.1±0.1	90±1	0.33±0.05	1.7(6)	0.12(4)
		$^{[4]}$B	0±0.5	0.3*	1*	10±1			

* value fixed during simulation

the dotted line which was drawn through the data of MacDonald and Hawthorne (1995) for which $^{[4]}$B = 0.0 a.p.f.u. (Lussier *et al.*, 2009). The present data are in closer accord with the dotted line of Fig. 7*a*, but are not decisive in choosing between the two relations, given that some of the data shown may not be reliable.

Oxidation state of Fe

The Mössbauer spectrum of the green Fe-rich rim (SHWGC: Table 5, Fig. 6) was fit by a two-site model, corresponding to Fe^{2+} and Fe^{3+} in octahedral coordination at the *Y*-site (Table 7), and representing different local short-range arrangements. Doublets with low δ and Δ values, such as those for Site 2 have often been attributed to $^{[4]}Fe^{3+}$. This issue was investigated in detail by Andreozzi *et al.* (2008) who concluded, through comparison of structural and Mössbauer data on many samples, that doublets with low δ and Δ values do not correspond to $^{[4]}Fe^{3+}$ in tourmalines, but rather to octahedrally coordinated Fe^{3+}.

The *Z* site was initially assigned as completely occupied by Al in the refinement process, and the equivalent isotropic-displacement parameters (U_{eq}) are in reasonable accord with equal scattering at the *Z* site in all of the structures refined here, i.e. 0.0070−0.0099 Å^2. The <*Z*−O> distances for all eight refined structures are between 1.902 and 1.906 Å, with a grand mean value of 1.904(2) Å. This value is in accord with the grand mean value of 1.905(1) Å for 26 refined liddicoatite structures given by Lussier *et al.* (2011) in which the *Z* sites were considered to be fully occupied by Al. Thus we conclude that the *Z* site is completely occupied by Al.

The *Y*-site populations were assigned from the unit formulae given in Table 5, and are in accord

TABLE 7. Room-temperature Mössbauer parameters* for the 'green cap' layer of Mogok wheatsheaf tourmaline.

SHW1-GC	δ (mm/s)	Δ (mm/s)	Rel. area (%)
Fe^{2+}	1.09	2.38	95(2)
Fe^{3+}	0.16	0.46	5(2)

* calibrated on α-Fe

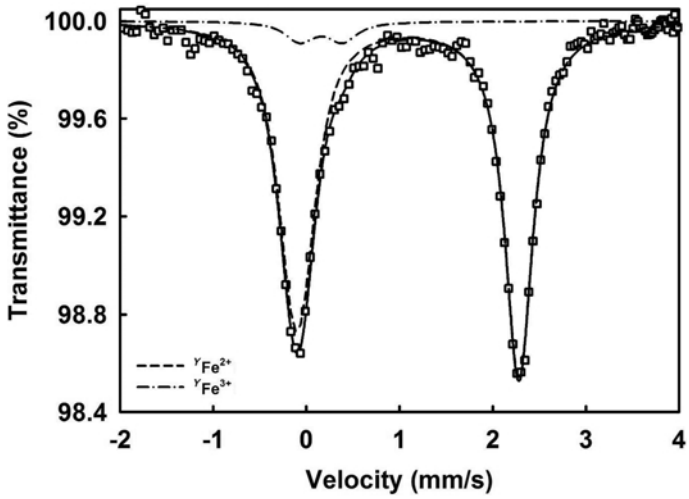

FIG. 6. Mössbauer spectrum of the thin 'green-cap' layer of wheatsheaf tourmaline.

with the refined site-scattering values (Table 4). The <*Y*–O> distance shows a well developed linear correlation with the aggregate ionic radius of *Y*-site constituents, r(*Y*) (Fig. 7*b*: <*Y*–O> = 0.65(5) <r[*Y*]> + 1.58(3), R = 0.965, standard error of estimate = 0.0028 Å), supporting the final site assignments.

The *X* site is occupied by Na and Ca, with significant vacancy. However, the green region of the sample (SHWGC and 3SHWGr) has nearly full occupancy of the *X* site. Final site-populations were assigned from the unit formulae (Table 5) and are compatible with the refined site-scattering values (Table 4).

Compositional zoning in wheatsheaf tourmaline

Two traverses of compositional data were collected along the profiles shown in Fig. 1*d*: Traverse 1 (red dots) across the central region of the crystal, and Traverse 2 (green dots) at the edge of the sample. Figures 8 and 9 summarize the cation variation with increasing distance from the start of each traverse. The abundance of transition metals correlates strongly with the red colour of the crystal (cf. Figs 1, 8 and 9), the white regions having <~0.02 a.p.f.u. transition metals. Inspection of Figs 8 and 9 shows that variation in $^{[4]}$B content plays a major role in chemical variation throughout this crystal. From the start of

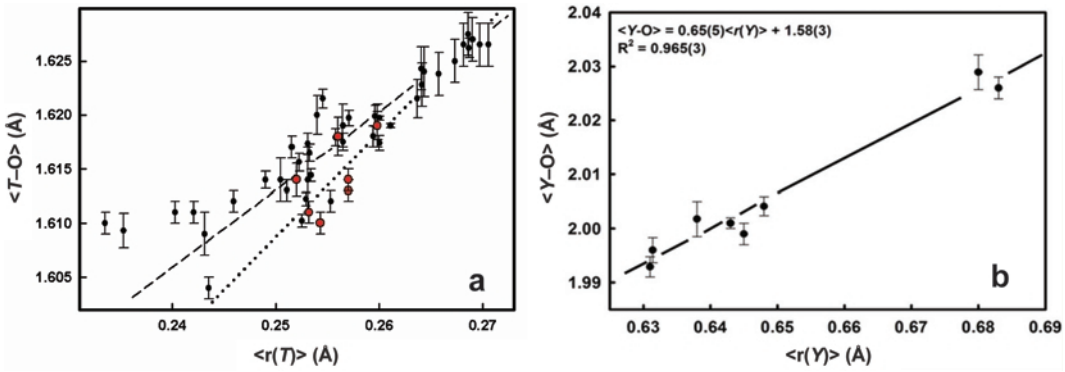

FIG. 7. (*a*) Variation in <*T*–O> distance as a function of the aggregate radius of the cations at the *T* site for the eight single crystals of wheatsheaf tourmaline (red circles) superimposed on a plot of literature data given by Lussier *et al.* (2011); (*b*) variation in <*Y*–O> distance as a function of the aggregate radius of the cations at the *Y* site for the eight single crystals of wheatsheaf tourmaline investigated in this study.

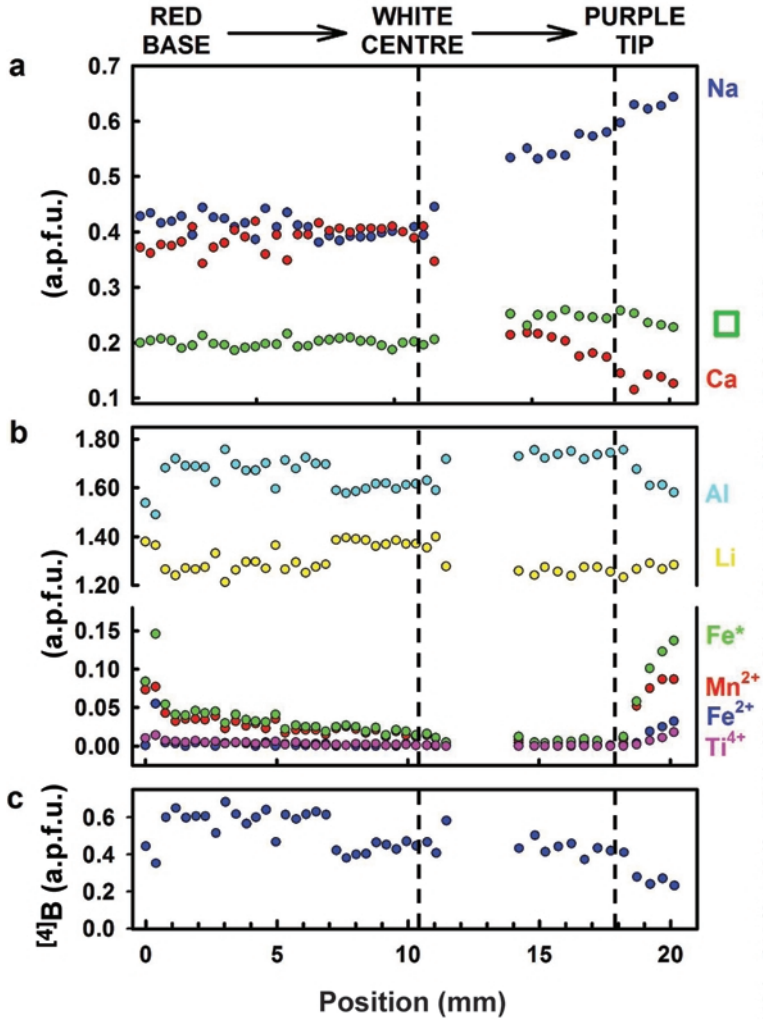

FIG. 8. Variation in chemical composition of wheatsheaf tourmaline composition along Traverse 1 (see Fig. 1*d*): (*a*) *X* site; (*b*) *Y* site; and (*c*) $^{[4]}$B at *T* site.

Traverse 1, $^{[4]}$B rises abruptly from 0.4 to 0.6 a.p.f.u. and ^{Y}Al rises from 1.5 to 1.7 a.p.f.u. while Fe* (= Fe^{2+} + Mn^{2+} + Ti) falls from 0.15 to 0.04 a.p.f.u. and Li falls from 1.4 to 1.2 a.p.f.u. Along the traverse, $^{[4]}$B declines to ~0.20 a.p.f.u. at the rim of the crystal *via* a series of discontinuous changes that shows analogous variations in Al, Li and, to a lesser extent, Fe*. These discontinuous changes in *T*- and *Y*-site occupancies are accompanied by little or no change in the *X*-site occupancies in the first half of the traverse. At the base of the crystal, Ca is slightly less than Na (both close to 0.4 a.p.f.u.) and the two converge halfway along the traverse, with the vacancy content, $^{X}\square$, constant at 0.2 p.f.u. Close to the middle of the traverse (the broken line marked WHITE CENTRE in Fig. 8), Ca begins to decrease sharply and Na begins to increase sharply, reaching 0.12 and 0.66 a.p.f.u., respectively, at the edge of the crystal. These changes in Na and Ca are smooth and show no abrupt change that correlates with the sharp rise in Fe* and drop in ^{Y}Al and $^{[4]}$B close to the edge of the crystal (at the second broken line in Fig. 8).

Traverse 2 shows a similar picture. Discontinuities in $^{[4]}$B correlate with similar changes in Al and Li, but not Fe* (see dotted

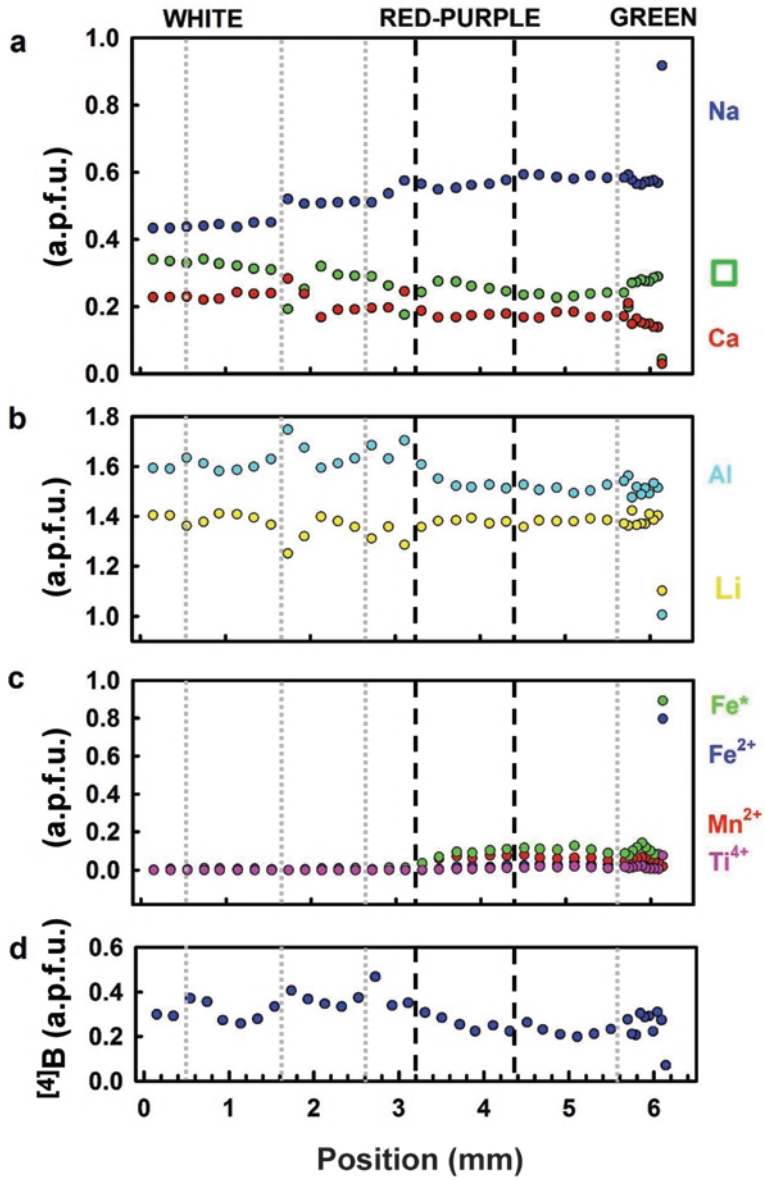

FIG. 9. Variation in the chemical composition of wheatsheaf tourmaline along Traverse 2 (see Fig. 1*d*): (*a*) *X* site; (*b*) Al and Li at the *Y* site; (*c*) transition metals at the *Y* site; and (*d*) $^{[4]}$B at the *T* site.

lines in Fig. 9) There is one analytical point in the green rim, and this shows a major compositional discontinuity with the rest of the crystal. Ca and $^{X}\square$ fall close to zero and Na exceeds 0.9 a.p.f.u. Fe* rises sharply from <0.1 a.p.f.u. to 0.9 a.p.f.u., both Al and Li fall to close to 1 a.p.f.u. each, and $^{[4]}$B drops from ~0.3 to <0.1 a.p.f.u.

Compositional variation in wheatsheaf tourmaline

Inspection of Figs 8 and 9 shows what initially appears as scatter in the variation of $^{[4]}$B as a function of distance. Plotting major constituents as a function of either $^{[4]}$B or ^{Y}Li (Figs 10 and 11) shows that this is not the case: major constituents

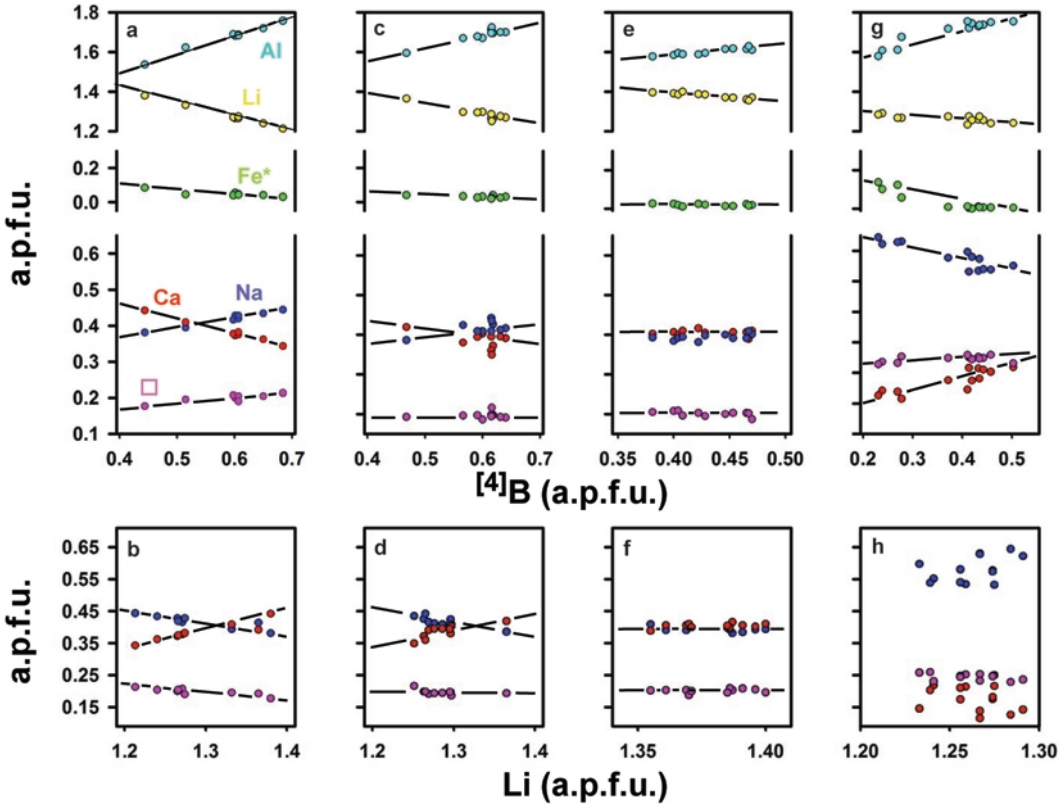

FIG. 10. Variation in major *X*-site and *Y*-site constituents as a function of $^{[4]}$B and ^{Y}Li along Traverse 1 of wheatsheaf tourmaline (red dots in Fig. 1*d*, see also Fig. 8): (*a*,*b*) 0.0 to 3.2 mm; (*c*,*d*) 3.2 to 6.9 mm; (*e*,*f*) 6.9 to 11.1 mm: (*g*,*h*) 14.2 to 20.2 mm.

vary in a linear manner such that this compositional change may be described by series of coupled substitutions. Prior to determining which substitutions are operative, the spatial profiles must be divided into regions with coherent substitution character; this is shown in Figs 10 and 11. Six substitutions are required to explain the variation observed in Figs 10 and 11, although not all of these operate simultaneously. For each region, the relevant substitutions, the amounts of each substitution p.f.u. and the corresponding distances along the spatial profiles, are summarized in Table 8.

All regions of the crystal show well developed, linear relations for ^{Y}Al, ^{Y}Li, and ^{Y}Fe* (Fe* = Fe^{2+} + Mn^{2+} + Mg) as a function of $^{[4]}$B, such that the principal substitutions accommodating the variation in *T*-site constituents are:

$$(1)\quad {}^{[4]}B_2 + {}^{Y}Al \rightarrow Si_2 + {}^{Y}Li$$

$$(2)\quad {}^{[4]}B + {}^{Y}Al \rightarrow Si + {}^{Y}Fe^{*}$$

In nearly every region, (1) and (2) couple with additional substitutions to accommodate compositional variation at the *X* site.

Figure 10*a*,*b* shows the compositional variation for the red core region of the sample, from 0.0 to 3.0 mm along the profile in Fig. 8. Here, substitutions (1) and (2) proceed for 0.10 and 0.05 p.f.u., respectively (Fig. 10*a*). Additionally, Fig. 10*b* shows that the *X*-site constituents also vary linearly with ^{Y}Li along the following substitutions (numbers in brackets indicate the amounts in p.f.u.):

$$(3)\quad {}^{X}\square + {}^{Y}Al \rightarrow {}^{X}Ca + {}^{Y}Li \qquad (0.04)$$
$$(4)\quad {}^{X}Na_2 + {}^{Y}Al \rightarrow {}^{X}Ca_2 + {}^{Y}Li \qquad (0.03)$$

In the white central region of the wheatsheaf crystal, from 3.2 to 6.9 mm in Fig. 8, substitutions (1) and (2) remain active (Fig. 10*c*) with amounts

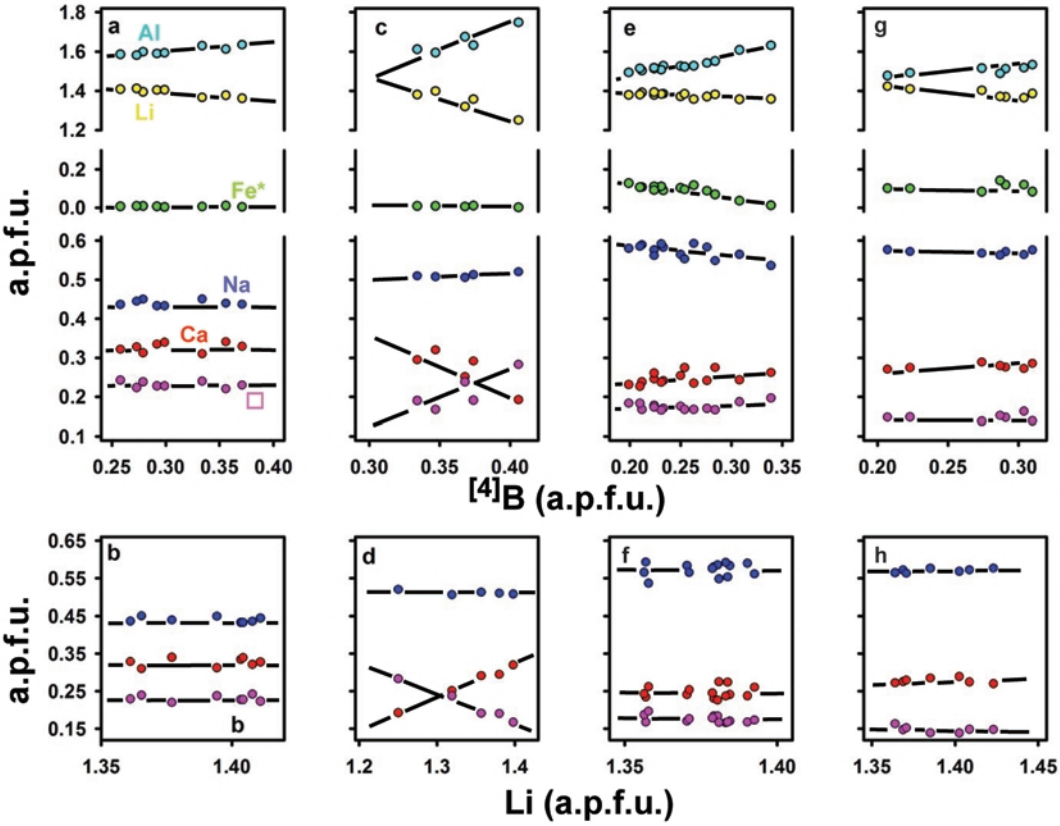

FIG. 11. Variation in major *X*-site and *Y*-site constituents as a function of $^{[4]}$B and ^{Y}Li along Traverse 2 of wheatsheaf tourmaline (green dots in Fig. 1*d*): (*a*,*b*) 0.0 to 1.5 mm; (*c*,*d*) 1.5 to 2.5 mm; (*e*,*f*) 2.5 to 5.7 mm: and (*g*,*h*) 5.7 to 6.1 mm.

of 0.07 and 0.01 p.f.u., respectively. Additional substitutions are required to maintain the compositional balance that must involve the *X*- and *Y*-site constituents. In contrast to the red base region, here the trends relating the variation in *X*- and *Y*-site constituents to *T*- and/or *Y*-site constituents are less obvious, given the amount of scatter about the ideal lines shown in Fig. 10*c*,*d*; the substitution may only be approximated as:

(5) ^{X}Na + ^{Y}Al + ^{T}B → ^{X}Ca + ^{Y}Li + ^{T}Si (0.03)

Between 6.9 and 11.1 mm in Fig. 8, which is still in the white region of the sample, there is no appreciable change in *X*-site composition and Fe* is ~0 a.p.f.u. throughout the region (Fig. 10*e*,*f*). Hence only substitution (1) is operative, with an amount of 0.05 p.f.u.

Toward the darker edge of the wheatsheaf sample (Fig. 10*g*,*h*), between 14.2 and 20.2 mm on the traverse shown in Fig. 8, there is considerable scatter in the data and Fig. 10*h* shows no discernible relation between the *Y*- and *X*-site constituents; hence only the variations in *X*- and *T*-site constituents are coupled. In this region, the variation in Na changes sign with respect to $^{[4]}$B when compared to the other regions of the wheatsheaf sample and the composition varies according to the following three substitutions:

(1) $^{[4]}B_2 + {}^{Y}Al \rightarrow Si_2 + {}^{Y}Li$ (0.03)
(2) $^{[4]}B + {}^{Y}Al \rightarrow Si + {}^{Y}Fe^*$ (0.13)
(6) $^{X}Ca + {}^{[4]}B \rightarrow {}^{X}Na + Si$ (0.09)

Figure 11*a*–*h* shows the compositional variation along Traverse 2 (shown in Fig. 9), which ends at a crystal face. From 0.0 to 1.5 mm, there is no variation in *X*-site constituents (Fig. 11*a*,*b*), and substitution (1) (0.05 p.f.u.) accounts for all the observed variation.

Between 1.5 and 2.5 mm (Fig. 11*c*), substitution (1) remains active (0.03 p.f.u.). In addition, a

TABLE 8. Substitution mechanisms and amounts (a.p.f.u.) for Mogok wheatsheaf tourmaline.

Red base (0.0 to 3.2 mm in Fig. 8)		
(1)	$^{Y}Al + {}^{T}B_2 \rightleftharpoons {}^{Y}Li + Si_2$	0.10
(2)	$^{Y}Al + {}^{T}B \rightleftharpoons {}^{Y}Fe^{*} + Si$	0.05
(3)	$^{X}\square + {}^{Y}Al \rightleftharpoons {}^{X}Ca + {}^{Y}Li$	0.04
(4)	$^{X}Na_2 + {}^{Y}Al \rightleftharpoons {}^{X}Ca_2 + {}^{Y}Li$	0.03
White core (3.2 to 6.9 mm in Fig. 8)		
(1)	$^{Y}Al + {}^{T}B_2 \rightleftharpoons Li + {}^{T}Si_2$	0.07
(2)	$^{Y}Al + {}^{T}B \rightleftharpoons Fe^{*} + {}^{T}Si$	0.01
(5)	$^{X}Na + {}^{Y}Al + {}^{T}B \rightleftharpoons {}^{X}Ca + {}^{Y}Li + Si$	0.03
White core (6.9 to 11.1 mm in Fig. 8)		
(1)	$^{Y}Al + {}^{T}B_2 \rightleftharpoons {}^{Y}Li + Si_2$	0.05
Dark edge (14.2 to 20.2 mm in Fig. 8)		
(1)	$^{Y}Al + {}^{T}B_2 \rightleftharpoons {}^{Y}Li + Si_2$	0.03
(2)	$^{Y}Al + {}^{T}B \rightleftharpoons {}^{Y}Fe^{*} + Si$	0.13
(6)	$^{X}Ca + {}^{T}B \rightleftharpoons {}^{X}Na + Si$	0.09
End (0.0 to 1.5 mm in Fig. 9)		
(1)	$^{Y}Al + {}^{T}B_2 \rightleftharpoons {}^{Y}Li + Si_2$	0.05
End (1.5 to 2.5 mm in Fig. 9)		
(1)	$^{Y}Al + {}^{T}B_2 \rightleftharpoons {}^{Y}Li + Si_2$	0.03
(3)	$^{X}\square + {}^{Y}Al \rightleftharpoons {}^{X}Ca + {}^{Y}Li$	0.10
(5)	$^{X}Na + {}^{Y}Al + {}^{T}B \rightleftharpoons {}^{X}Ca + {}^{Y}Li + Si$	0.01
End (2.5 to 5.7 mm in Fig. 9)		
(1)	$^{Y}Al + {}^{T}B_2 \rightleftharpoons {}^{Y}Li + Si_2$	0.01
(2)	$^{Y}Al + {}^{T}B \rightleftharpoons {}^{Y}Fe^{*} + Si$	0.12
(6)	$^{X}Ca + {}^{T}B \rightleftharpoons {}^{X}Na + Si$	0.02
End (5.7 to 6.1 mm in Fig. 9)		
(1)	$^{Y}Al + {}^{T}B_2 \rightleftharpoons {}^{Y}Li + Si_2$	0.04
(2)	$^{Y}Al + {}^{T}B \rightleftharpoons {}^{Y}Fe + Si$	0.02

well developed linear relation between *X*- and *Y*-site constituents (Fig. 11*d*) indicates that substitutions (3) and (5) are active,

(3) $^{X}\square + {}^{Y}Al \rightarrow {}^{X}Ca + {}^{Y}Li$ (0.10)
(5) $^{X}Na + {}^{Y}Al + {}^{[4]}B \rightarrow {}^{X}Ca + {}^{Y}Li + Si$ (0.01)

Between 2.5 and 5.7 mm (Fig. 11*e*,*f*), substitution (1) is active (0.01 p.f.u.) and substitution (2), which accounts for the entire variation in Fe*, is active (0.12 p.f.u.). There is no correlation between *Y*- and *X*-site constituents. As observed in Fig 10*g*, there is a decrease in Na as a function of $^{[4]}B$, corresponding to

(6) $^{X}Ca + {}^{[4]}B \rightarrow {}^{X}Na + Si$ (0.02).

Between 5.7 and 6.1 mm (Fig. 11*g*,*h*), there is effectively no change in *X*-site constituents, and the composition varies according to substitutions (1) (0.04 a.p.f.u.) and (2) (0.02 p.f.u.).

Growth of wheatsheaf tourmaline

At the base of the sample in the reddish region visible in Fig. 1*b*, there is a single crystal flanked by lighter-coloured material to either side (Fig. 2*a*). The width of this crystal increases in the *c* direction, and a high-magnification image (Fig. 2*b*) shows that the central core crystal splits (bifurcates) into multiple crystals which again bifurcate and increase in width along the *c* direction. Continued bifurcation and growth has imparted a non-planar aspect to the outer surface of the crystal aggregate (Fig. 2*c*) which results in the overall 'wheatsheaf' shape that is observed (Fig. 1*a*).

The red core and surrounding colourless crystal that constitute the bulk of the aggregate (Fig. 1*b*,*c*) show a gradual decrease in Fe* to <0.02 a.p.f.u. in the direction of growth parallel to *c*, suggesting crystallization from a continuously differentiating parent fluid without any abrupt change in composition of the latter. The purplish-red rind toward the edge of the crystal aggregate (Fig. 1*c*) shows a gradual increase in Fe* in the direction of growth. This compositional change is rather unusual, as Fe* contents of elbaitic tourmaline tend to decrease with progressive crystallization (e.g. as in the central regions of this crystal, and in the mushroom tourmalines of Mogok, Lussier *et al.*, 2008*a*,*b*). It seems reasonable to suggest that an external Fe-rich fluid began to leak into the miarolitic cavity and the gross fluid composition began to evolve towards a more Fe-rich composition with the crystallizing tourmaline becoming more Fe-rich as the fluid composition evolved. This period terminated with breaching of the cavity and a sudden increase in Fe in the fluid, with crystallization of the green cap of Fe-rich elbaite (Fig. 10*c*) in which the Fe* content reaches ~0.90 a.p.f.u.

Bifurcation as a process in the growth of tourmaline

A feature of particular interest in this study is the role of crystal bifurcation in tourmaline growth and its role in affecting crystal habit. Lussier *et al.* (2008*a*,*b*, 2011, this work) and Lussier and Hawthorne (2011) have examined in detail the

compositional and textural features of three very different habits of tourmaline: (1) mushroom tourmaline from Mogok, Myanmar; (2) oscillatory zoned tourmaline from Madagascar; and (3) wheatsheaf tourmaline from Mogok. The oscillatory zoned tourmaline from Madagascar showed no sign of crystallite bifurcation, the tourmaline crystals are prismatic and the external prism faces are parallel. Mushroom tourmaline from Mogok shows extensive crystallite bifurcation and the unusual mushroom habit is the macroscopic expression of the underlying bifurcated microstructure. Wheatsheaf tourmaline is intermediate between the first two examples; it has an intermediate amount of bifurcation that gives rise to the wheatsheaf habit at the macroscopic level. We are currently examining the possible changing conditions that give rise to bifurcation of crystals during growth. We note that divergent crystal aggregates are common in elbaitic tourmalines from pegmatites, and suggest that crystal bifurcation is the mechanism by which such habits form.

Summary

(1) MAS NMR spectroscopy shows the presence of $^{[4]}$B and $^{[4]}$Al throughout the wheatsheaf sample. Spectral simulation and peak fitting yield mean values of 0.30 and <0.12 a.p.f.u. for $^{[4]}$B and $^{[4]}$Al, respectively.

(2) There is good agreement between the quantities of $^{[4]}$B derived from simulation of ^{11}B MAS NMR spectra and unit-formula normalization of EMPA data based on 31 anions with (OH + F) = 4 a.p.f.u., Si + B = 9 a.p.f.u., and Li = $15 - \Sigma(Y + Z + T)$ a.p.f.u., suggesting that $^{[4]}$Al is a minor constituent in wheatsheaf tourmaline, in accord with the ^{27}Al MAS NMR spectra.

(3) Mössbauer spectroscopy shows that Fe^{2+} is the only Fe species in the dark green end of the sample.

(4) Major compositional variation in the wheatsheaf sample involves the substitutions $^{[4]}$B + ^{Y}Al → Si + ^{Y}Fe* where transition metals are present, and $^{[4]}B_2$ + ^{Y}Al → Si_2 + ^{Y}Li where transition metals are not present.

(5) Successive bifurcation of crystallites causes divergence of growth directions along the *c* axis, imparting an overall 'wheatsheaf' shape to the crystal aggregate.

(6) We suggest that such bifurcation is common in pegmatitic elbaite crystals, resulting in their common divergent habit.

Acknowledgements

We are indebted to Drs Gianni Andreozzi and Gerhard Franz for their comments on this paper. We thank Drs Victor Terskih and Shane Pawsey for technical assistance at the ultrahigh-field facility. This work was funded by an NSERC PGS-D, a University of Manitoba Graduate Fellowship, and a Manitoba Graduate Scholarship to AJL and VKM, by a University of Manitoba Graduate Fellowship to SH, by Major Facilities Access grants to FCH, and by Research Tools and Equipment, and Discovery grants to FCH and SK from the Natural Sciences and Engineering Research Council of Canada, and by Canada Foundation for Innovation grants to FCH and SK. Access to the 900 MHz NMR spectrometer was provided by the National Ultrahigh Field NMR Facility for Solids (Ottawa, Canada), a national research facility funded by the Canada Foundation for Innovation, the Ontario Innovation Trust, Recherche Québec, the National Research Council of Canada and Bruker BioSpin, and managed by the University of Ottawa (www.nmr900.ca).

References

Andreozzi, G.B., Bosi, F. and Longo, M. (2008) Linking Mössbauer and structural parameters in elbaite-schorl-dravite tourmalines. *American Mineralogist*, **93**, 658–666.

Aurisicchio, C., Ottolini, L. and Pezzotta, F. (1999) Electron- and ion-microprobe analyses, and genetic inferences of tourmalines of the foitite-schorl solid solution. *European Journal of Mineralogy*, **11**, 217–225.

Barley, M., Pickard, A.L. and Zaw, K. (2003) Jurassic to Miocene magmatism and metamorphism in the Mogok metamorphic belt and the India-Eurasia collision in Myanmar. *Tectonics*, **22**, 1019–1031.

Bloodaxe, E.S., Hughes, J.M., Dyar, M.D., Grew, E.S. and Guidotti, C.V. (1999) Linking structure and chemistry in the schorl-dravite series. *American Mineralogist*, **84**, 922–928.

Bosi, F. (2008) Disordering of Fe^{2+} over octahedrally coordinated sites of tourmaline. *American Mineralogist*, **93**, 1647–1653.

Bosi, F. and Lucchesi, S. (2004) Crystal chemistry of the schorl-dravite series. *European Journal of Mineralogy*, **16**, 335–344.

Bosi, F. and Lucchesi, S. (2007) Crystal chemistry in the tourmaline group: Structural constraints on chemical variability. *American Mineralogist*, **92**, 1054–1063.

Bosi, F., Andreozzi, G.B., Federico, M., Graziani, G.

and Lucchesi, S. (2005) Crystal chemistry of the elbaite-schorl series. *American Mineralogist*, **90**, 1784–1792.

Bosi, F., Lucchesi, S. and Reznitskii L. (2004) Crystal chemistry of the dravite–chromdravite series. *European Journal of Mineralogy*, **16**, 345–352.

Bray, P.J. (1999) NMR and NQR studies of boron in vitreous and crystalline borates. *Inorganica Chimica Acta*, **289**, 158–173.

Burns, P.C., Macdonald, D.J. and Hawthorne, F.C. (1994) The crystal chemistry of manganese-bearing elbaite. *The Canadian Mineralogist*, **32**, 31–41.

Cámara, F., Ottolini, L. and Hawthorne, F.C. (2002) Crystal chemistry of three tourmalines by SREF, EMPA, and SIMS. *American Mineralogist*, **87**, 1437–1442.

Dyar, M.D., Taylor, M.E., Lutz, T.M., Francis, C.A., Robertson, J.D., Cross, L.M., Guidotti, C.V. and Wise, M. (1998) Inclusive chemical characterization of tourmaline: Mössbauer study of Fe valence and site occupancy. *American Mineralogist*, **83**, 848–864.

Ertl, A. and Hughes, J.M. (2002) The crystal structure of an aluminum-rich schorl overgrown by boron-rich olenite from Koralpe, Styria, Austria. *Mineralogy and Petrology*, **75**, 69–78.

Ertl, A., Hughes, J.M., Brandstätter, F., Dyar, M.D. and Prasad, P.S.R. (2003*a*) Disordered Mg-bearing olenite from a granitic pegmatite from Goslarn, Austria: A chemical, structural, and infrared spectroscopic study. *The Canadian Mineralogist*, **41**, 1363–1370.

Ertl, A., Hughes, J.M., Prowatke, S., Rossman, G.R., London, D. and Fritz, E.A. (2003*b*) Mn-rich tourmaline from Austria: structure, chemistry, optical spectra, and relations to synthetic solid solutions. *American Mineralogist*, **88**, 1369–1376.

Ertl, A., Pertlik, F., Dyar, M.D., Prowatke, S., Hughes, J.M., Ludwig, T. and Bernhardt, H.-J. (2004) Fe-rich olenite with tetrahedrally coordinated Fe^{3+} from Eibenstein, Austria: Structural, chemical, and Mössbauer data. *The Canadian Mineralogist*, **42**, 1057–1063.

Ertl, A., Rossman, G.R., Hughes, J.M., Prowatke, S. and Ludwig, T. (2005) Mn-bearing "oxy-rossmanite" with tetrahedrally coordinated Al and B from Austria: Structure, chemistry, and infrared and optical spectroscopic study. *American Mineralogist*, **90**, 481–487.

Ertl, A., Hughes, J.M., Prowatke, S., Ludwig, T., Brandstatter, F., Korner, W. and Dyar, M.D. (2007) Tetrahedrally coordinated boron in Li-bearing olenite from ''Mushroom'' tourmaline from Momeik, Myanmar. *The Canadian Mineralogist*, **45**, 891–899.

Francis, C.A., Dyar, M.D., Williams, M.L. and Hughes, J.M. (1999) The occurrence and crystal structure of foitite from a tungsten-bearing vein at Copper Mountain, Taos County, New Mexico. *The Canadian Mineralogist*, **37**, 1431–1438.

Grice, J.D. and Ercit, T.S. (1993) Ordering of Fe and Mg in the tourmaline crystal structure: the correct formula. *Neues Jahrbuch für Mineralogie Abhandlungen*, **165**, 245–266.

Grice, J.D., Ercit, T.S. and Hawthorne, F.C. (1993) Povondraite, a redefinition of the tourmaline ferridravite. *American Mineralogist*, **78**, 433–436.

Hawthorne, F.C. (1996) Structural mechanisms for light-element variations in tourmaline. *The Canadian Mineralogist*, **34**, 123–132.

Hawthorne, F.C. (2002) Bond-valence constraints on the chemical composition of tourmaline. *The Canadian Mineralogist*, **40**, 789–798.

Hawthorne, F.C. and Henry, D.J. (1999) Classification of the minerals of the tourmaline group. *European Journal of Mineralogy*, **11**, 201–215.

Hawthorne, F.C., Macdonald, D.J. and Burns, P.C. (1993) Reassignment of cation site occupancies in tourmaline: Al-Mg disorder in the crystal structure of dravite. *American Mineralogist*, **78**, 265–270.

Hawthorne, F.C., Ungaretti, L. and Oberti, R. (1995) Site populations in minerals: terminology and presentation of results of crystal-structure refinement. *The Canadian Mineralogist*, **33**, 907–911.

Hawthorne, F.C., Burns, P.C. and Grice, J.D. (1996) The crystal chemistry of boron. Pp. 41–115 in: *Boron: Mineralogy, Petrology and Geochemistry* (E.S. Grew and L.M. Anovitz, editors). Reviews in Mineralogy, **33**, Mineralogical Society of America, Washington, D.C.

Henry, D.J. and Dutrow, B.L. (1992) Tourmaline in low-grade clastic sedimentary rocks: an example of the petrogenetic potential of tourmaline. *Contributions to Mineralogy and Petrology*, **112**, 203–218.

Henry, D.J. and Dutrow, B.L. (1996) Metamorphic tourmaline and its petrogenetic applications. Pp. 503–557 in: *Boron: Mineralogy, Petrology and Geochemistry* (E.S. Grew and L.M. Anovitz, editors). Reviews in Mineralogy, **33**, Mineralogical Society of America, Washington, D.C.

Henry, D.J. and Guidotti, C.V. (1985) Tourmaline as a petrogenetic indicator mineral: an example from the staurolite-grade metapelites of NW Maine. *American Mineralogist*, **70**, 1–15.

Hla Kyi, U., Themelis, T. and Kyaw Thu, U. (2005) The pegmatitic deposits of Molo (Momeik) and Sakan-Gya (Mogok). *Australian Gemologist*, **22**, 303–309.

Hughes, J.M., Ertl, A., Dyar, M.D., Grew, E.S., Shearer, C.K., Yates, M.G. and Guidotti, C.V. (2000) Tetrahedrally coordinated boron in a tourmaline: boron-rich olenite from Stoffhütte, Koralpe, Austria. *The Canadian Mineralogist*, **38**, 861–868.

Hughes, J.M., Ertl, A., Dyar, M.D., Grew, E.S., Wiedenbeck, M. and Brandstätter, F. (2004) Structural and chemical response to varying $^{[4]}$B content in zoned Fe-bearing olenite from Koralpe, Austria. *American Mineralogist*, **89**, 447–454.

Kroeker, S. and Stebbins, J.F. (2001) Three-Coordinated Boron-11 Chemical Shifts in Borates. *Inorganic Chemistry*, **40**, 6239–6246.

Lussier, A. and Hawthorne, F.C. (2011) Oscillatory zoned liddicoatite from central Madagascar. II. Compositional variation and substitution mechanisms. *The Canadian Mineralogist*, **49**, 89–104.

Lussier, A.J., Aguiar, P.M., Michaelis, V.K., Kroeker, S., Herwig, S., Abdu, Y. and Hawthorne, F.C., (2008*a*) Mushroom elbaite from the Kat Chay mine, Momeik, near Mogok, Myanmar: I. Crystal chemistry by SREF, EMPA, MAS NMR and Mössbauer spectroscopy. *Mineralogical Magazine*, **72**, 747–761.

Lussier, A.J., Hawthorne, F.C., Herwig, S., Abdu, Y., Aguiar, P.M., Michaelis, V.K. and Kroeker, S. (2008*b*) Mushroom elbaite from the Kat Chay mine, Momeik, near Mogok, Myanmar: II. Zoning and crystal growth. *Mineralogical Magazine*, **72**, 999–1010.

Lussier, A.J., Aguiar, P., Michaelis, V., Kroeker, S. and Hawthorne, F.C. (2009) The occurrence of tetrahedrally coordinated Al and B in tourmaline: An ^{11}B and ^{27}Al MAS NMR study. *American Mineralogist*, **94**, 785–792.

Lussier, A., Abdu, Y., Hawthorne, F.C., Michaelis, V.K., Aguiar, P.M. and Kroeker, S. (2011) Oscillatory zoned liddicoatite from central Madagascar. I. Crystal chemistry and structure by SREF and ^{11}B and ^{27}Al MAS NMR spectroscopy. *The Canadian Mineralogist*, **49**, 63–88.

Macdonald, D.J. and Hawthorne, F.C. (1995) The crystal chemistry of Si-Al substitution in tourmaline. *The Canadian Mineralogist*, **33**, 849–858.

Macdonald, D.J., Hawthorne, F.C. and Grice, J.D. (1993) Foitite, $\square[Fe^{2+}_2(Al,Fe^{3+})]Al_6Si_6O_{18}(BO_3)_3(OH)_4$, a new alkali deficient tourmaline: description and crystal structure. *American Mineralogist*, **78**, 1299–1303.

Marler, B. and Ertl, A. (2002) Nuclear magnetic resonance and infrared spectroscopic study of excess-boron olenite from Koralpe, Styria, Austria. *American Mineralogist*, **87**, 364–367.

Marschall, H.R., Ertl, A., Hughes, J.M. and McCammon, C. (2004) Metamorphic Na- and OH-rich disordered dravite with tetrahedral boron associated with omphacite, from Syros, Greece: chemistry and structure. *European Journal of Mineralogy*, **16**, 817–823.

Michaelis, V.K., Aguiar, P.M. and Kroeker, S. (2007) Probing alkali coordination environments in alkali borate glasses by multinuclear magnetic resonance. *Journal of Non-Crystalline Solids*, **353**, 2582–2590.

Neiva, A.M.R., Manuela, M., Silva, V.G. and Gomes, M.E. (2007) Crystal chemistry of tourmaline from Variscan granites, associated tin-tungsten- and gold deposits, and associated metamorphic and metasomatic rocks from northern Portugal. *Neues Jahrbuch für Mineralogie Abhandlungen*, **184**, 45–76.

Novák, M. and Povondra, P. (1995) Elbaite pegmatites in the Moldanubicum: a new subtype of the rare-element class. *Mineralogy and Petrology*, **55**, 159–176.

Novák, M., Selway, J., Černý, P., Hawthorne, F.C. and Ottolini, L. (1999) Tourmaline of the elbaite-dravite series from an elbaite-subtype pegmatite at Bliñná, southern Bohemia, Czech Republic. *European Journal of Mineralogy*, **11**, 557–568.

Pouchou, J.L. and Pichoir, F. (1985) 'PAP' φ(ρZ) procedure for improved quantitative microanalysis. Pp. 104–106 in: *Microbeam Analysis* (J.T. Armstrong, editor). San Francisco Press, San Francisco, California, USA.

Povondra, P. and Novák, M. (1986) Tourmalines in metamorphosed carbonate rocks from western Moravia, Czechoslovakia. *Neues Jahrbuch für Mineralogie Monatshefte*, **1986**, 273–282.

Schreyer, W., Wodara, U., Marler, B., Van Aken, P.A., Seifert, F. and Robert, J.-L. (2002) Synthetic tourmaline (olenite) with excess boron replacing silicon in the tetrahedral site: I. Synthesis conditions, chemical and spectroscopic evidence. *European Journal of Mineralogy*, **12**, 529–541.

Selway, J., Černý, P. and Hawthorne, F.C. (1998) Feruvite from lepidolite pegmatites at Red Cross Lake, Manitoba. *The Canadian Mineralogist*, **36**, 433–439.

Selway, J.B., Novák, M., Černý, P. and Hawthorne, F.C. (1999) Compositional evolution of tourmaline in lepidolite-subtype pegmatites. *European Journal of Mineralogy*, **11**, 569–584.

Selway, J.B., Novák, M., Černý, P. and Hawthorne, F.C. (2000*a*) The Tanco pegmatite at Bernic Lake, Manitoba. XIII. Exocontact tourmaline. *The Canadian Mineralogist*, **38**, 869–976.

Selway, J.B., Černý, P., Hawthorne, F.C. and Novák, M. (2000*b*) The Tanco pegmatite at Bernic Lake, Manitoba. XIV. Internal tourmaline. *The Canadian Mineralogist*, **38**, 877–891.

Selway, J.B., Smeds, S-A., Černý, P. and Hawthorne, F.C. (2002) Compositional evolution of tourmaline in the petalite-subtype Nyköpingsgruvan pegmatites, Utö, Stockholm Archipelago, Sweden. *GFF*, **124**, 93–102.

Sheldrick, G.M. (1998) *SADABS* User Guide, University of Göttingen, Germany.

Skibsted, J., Nielsen, N.C., Bildsøe, H. and Jakobsen, H.J. (1991) Satellite transitions in MAS NMR

spectra of quadrupolar nuclei. *Journal of Magnetic Resonance*, **95**, 88–117.

Tagg, S.L., Cho, H., Dyar, M.D. and Grew, E.S. (1999) Tetrahedral boron in naturally occurring tourmaline. *American Mineralogist*, **84**, 1451–1455.

Taylor, M.C., Cooper, M.A. and Hawthorne, F.C. (1995) Local charge-compensation in hydroxy-deficient uvite. *The Canadian Mineralogist*, **33**, 1215–1221.

Themelis, T. (2007) *Gems and Mines of Mogok: The Forbidden Land.* A & T Press, Bangkok, Thailand.

Zaw, K. (1998) Geological evolution of selected granitic pegmatites in Myanmar (Burma): constraints from regional setting, lithology, and fluid-inclusion studies. *International Geology Review*, **40**, 647–662.